nature geoscience

ARTICLES

PUBLISHED ONLINE: 1 AUGUST 2016 | DOI: 10.1038/NGEO2772

Redox-induced lower mantle density contrast and effect on mantle structure and primitive oxygen

Tingting Gu[1]*, Mingming Li[2†], Catherine McCammon[3] and Kanani K. M. Lee[1]

The mantle comprises nearly three-quarters of Earth's volume and through convection connects the deep interior with the lithosphere and atmosphere. The composition of the mantle determines volcanic emissions, which are intimately linked to evolution of the primitive atmosphere. Fundamental questions remain on how and when the proto-Earth mantle became oxidized, and whether redox state is homogeneous or developed large-scale structures. Here we present experiments in which we subjected two synthetic samples of nearly identical composition that are representative of the lower mantle (enstatite chondrite), but synthesized under different oxygen fugacities, to pressures and temperatures up to 90 GPa and 2,400 K. In addition to the mineral bridgmanite, compression of the more reduced material also produced Al_2O_3 as a separate phase, and the resulting assemblage is about 1 to 1.5% denser than in experiments with the more oxidized material. Our geodynamic simulations suggest that such a density difference can cause a rapid ascent and accumulation of oxidized material in the upper mantle, with descent of the denser reduced material to the core–mantle boundary. We suggest that the resulting heterogeneous redox conditions in Earth's interior can contribute to the large low-shear velocity provinces in the lower mantle and the evolution of atmospheric oxygen.

Evidence of Earth's redox history has been overwritten by the ongoing dynamics of our planet. The Great Oxidation Event (GOE), which marks the accumulation of substantial oxygen in the atmosphere, occurred ~2.3 Gyr ago and has been linked to the appearance of cyanobacteria and the rise of photosynthesis. However, multiple lines of evidence including biomarkers[1], Cr isotopes[2], and Mn oxidation[3] indicate an earlier oxidation of the surface (~2.7–3 Gyr ago), and the buffer reaction of mantle degassing with the atmosphere would have had a profound effect on the rise of O_2 (refs 4,5). The composition of volcanic gas emitted strongly depends on the oxygen fugacity (fO_2) of its source region. However, V/Sc ratios in basalts indicate nearly constant fO_2 (~FMQ (fayalite–magnetite–quartz buffer) −0.5) since the Archaean eon, suggesting a very small fO_2 increase of the parent source of mid-ocean ridge basalts (MORBs)[6]. Nevertheless, the fO_2 of Archaean rocks shows a broad range, with values for Archaean cratonic asthenosphere such as the Kaapvaal craton lower than FMQ −3.5 (ref. 7) and decreasing with depth[8]. How Earth reached its modern redox state either temporally or spatially is still an enigma.

Tracing back to the Earth's formation, it is generally assumed that the planet accreted from meteorites, and the primitive core and mantle formed from a magma ocean[9]. The nature of the redox conditions in Earth's interior can be controlled by redox-sensitive elements in its early history. As an abundant element, iron would undergo multiple reactions in the high temperatures of a magma ocean, such as the self-oxidation of ferrous iron to ferric and native iron[10]. However, it is unclear if the Fe^{2+}- and Fe^{3+}-bearing speciations crystallized under different fO_2 conditions would be segregated through mantle convection and developed into heterogeneous redox structures that potentially affect the redox evolution in Earth's deep interior. To understand this process, we investigated the mineral assemblages crystallized from the composition representative of the primitive state of the early mantle. Although the composition of the primitive mantle is difficult to ascertain, by comparing with meteorites—our best guess for the Earth's building blocks—enstatite chondrites make a good isotopic match for the Earth. Among enstatite chondrites, the iron-rich EH chondrite class (29–35% Fe) is considered more 'primitive' than the iron-poor EL class (20–29% Fe), as defined by petrological and textural characteristics[11]. Thus, we chose the lower-mantle model of Javoy[12], an average EH composition, as a possible composition of the primitive mantle. We synthesized our starting enstatite chondritic glasses with nearly identical bulk composition (Supplementary Table 1), but under different initial oxygen fugacities so that we could investigate the effect of fO_2 independently. The synthesis conditions led not only to slightly different ferric iron contents in the glasses, as measured by Mössbauer spectroscopy (Supplementary Fig. 1 and Supplementary Table 1), but possibly also to different oxygen contents and vacancy concentrations induced by non-stoichiometry. We compared their phase assemblages and equations of state using a laser-heated diamond-anvil cell (LHDAC) and synchrotron-based X-ray diffraction (XRD) through most of the pressure and temperature range of the lower mantle to study how fO_2 affects the density of these samples. Then, based on our laboratory measurements, we used geodynamic models to simulate the possible redox distribution and evolution in the mantle.

Redox state affects lower-mantle phase assemblage

Synchrotron-based XRD patterns revealed two minerals present in the enstatite chondrite lower-mantle model compositions for our experimental conditions (30–90 GPa, 1,800–2,400 K), that is, bridgmanite (Bm)[13] and SiO_2 silica as stishovite (Stv) or in the $CaCl_2$ structure (Supplementary Fig. 2). Ca-Pv was not observed as a single phase in the XRD patterns with low abundance

[1]Department of Geology & Geophysics, Yale University, New Haven, Connecticut 06511, USA. [2]School of Earth and Space Exploration, Arizona State University, Tempe, Arizona 85287, USA. [3]Bayerisches Geoinstitut, Universität Bayreuth, Bayreuth 95440, Germany. [†]Present address: Department of Physics, University of Colorado, Boulder, Colorado 80309, USA. *e-mail: gtt.pku@gmail.com

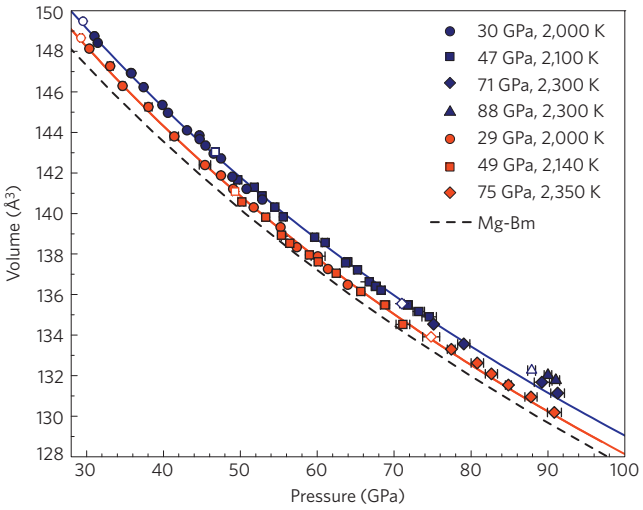

Figure 1 | Pressure versus volume of bridgmanite at room temperature, with corresponding Birch–Murnaghan equation of state curves. J95_RED (dark blue) and J95_OX (orange) samples are shown with $P_{Ne/Ar}$ for all the data (pressures measured according to the diffraction lines of Ne (ref. 34) or Ar (ref. 35) and their uncertainties are given by error bars). Open symbols indicate pressures at which the Bm were synthesized, followed by solid symbols for their subsequent development. A black dashed curve is shown for pure endmember $MgSiO_3$ Bm (ref. 14).

of Ca in the starting samples (<2 wt%), which should thus be dissolved in the Bm or below the detection limit. Furthermore, the common lower-mantle mineral ferropericlase (Mg,Fe)O was also not detected due to molar (Mg+Fe)/Si ~1 in the starting compositions (Supplementary Table 1). At ~88 GPa and 2,300 K, we observed a doublet near ~2.5 Å that could not be attributed to either Bm or SiO_2 in the J95_RED sample, and may be evidence for the start of the transition of Bm (that is, perovskite) to the post-perovskite structure. In addition, recovered samples were measured and their lattice parameters were obtained at ambient conditions (Supplementary Table 2).

The mineral assemblages and the lattice parameters of the two samples show subtle differences at high pressure as well as upon quenching to room pressure (Supplementary Table 2). The volumes of Bm in the more reduced J95_RED samples are slightly larger, that is, ~0.4%, than that of the more oxidized J95_OX samples (Fig. 1), and both are larger than the pure Mg-endmember Bm[14]. Stishovite peaks were observed in both samples, and are more pronounced in J95_RED, suggesting that the J95_OX sample has less free silica (as Stv) than J95_RED. After heating at 70 GPa and 2,300 K, $CaCl_2$-structured SiO_2 (110) peaks[15] were observed (Supplementary Fig. 2). The proportion of SiO_2 to Bm was calculated from samples quenched from pressures less than 50 GPa to ambient conditions, which shows about 4.2 (±0.5) wt% Stv in J95_RED and 1.9 (±0.3) wt% in J95_OX. The bulk modulus of Bm in the J95_RED sample (listed in Supplementary Table 2) is about 1.6% larger than that of sample J95_OX, which means the effect of ferric iron concentration on the bulk modulus of Bm is not significant, at least for lower-mantle pressures.

Recovered samples were examined by electron probe microanalysis (EPMA) (Supplementary Table 3) and show strikingly different features (Fig. 2 and Supplementary Fig. 3). Both samples show clear crystal grain boundaries on their surfaces (Supplementary Fig. 3), indicating that they were well insulated from the anvils. However, we observed that in the more reduced J95_RED samples, alumina Al_2O_3 with grain size less than ~5 μm were exsolved as a separate phase and distributed on the sample surface (Supplementary Fig. 3) as well as throughout the recovered sample, as observed in a cross-section cut by focused ion beam (FIB) (Fig. 2a). Alumina exsolution was observed in all J95_RED samples, whereas on the recovered J95_OX samples we did not observe any alumina grains (Fig. 2b). Using NIH ImageJ[16] we

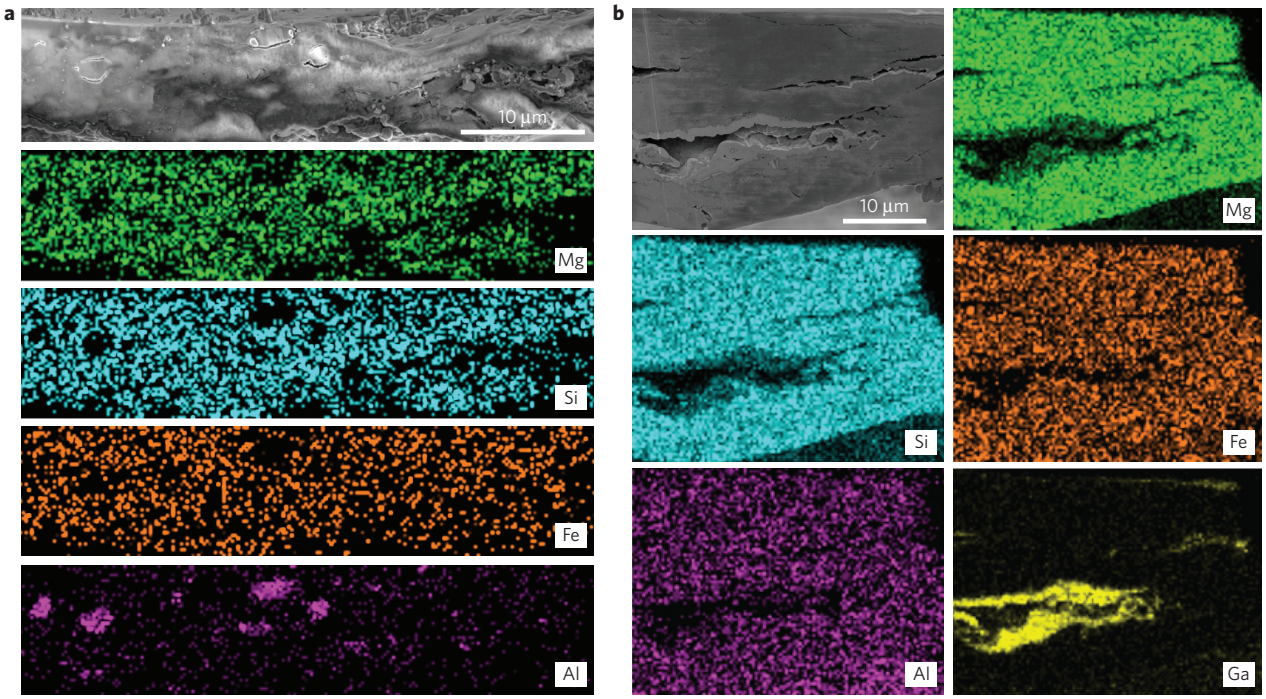

Figure 2 | Elemental mapping of Mg, Si, Fe, Al and Ga of quenched sample cross sections. a, J95_RED sample quenched from 88 GPa, 2,300 K. Note the composition map suggests several large Al_2O_3 grains amongst an otherwise homogeneous chemistry across the sample. **b**, J95_OX sample quenched from 75 GPa, 2,350 K. Ga aggregates around the edge of cracks during FIB processing. Note the homogeneity of the composition map across the sample.

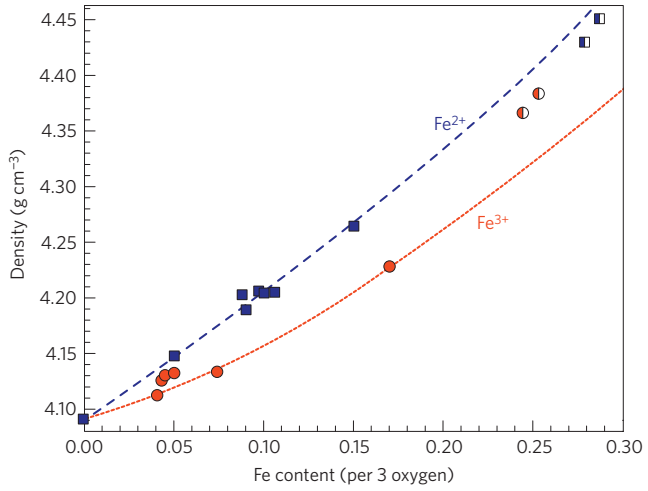

Figure 3 | Density of Bm at ambient conditions as a function of Fe content. Endmember $MgSiO_3$, Fe^{2+} substitution (blue squares), Fe^{3+} substitution (orange circles), and mixed Fe^{2+} and Fe^{3+} substitution (half square, J95_RED; half circle, J95_OX) Bm densities are shown. Data sources: Mg endmember, ref. 22; Fe^{2+}, refs 19,20,22–24; Fe^{3+}, refs 18,21. Dashed lines are guides for the eye.

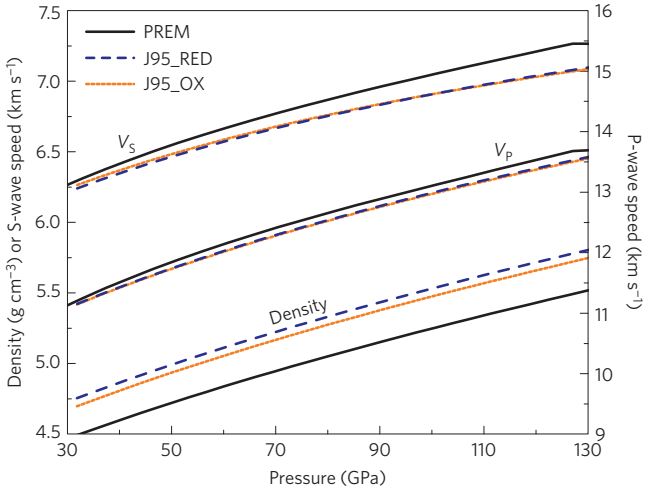

Figure 4 | Computed assemblage density, S-wave speed (V_S), and P-wave speed (V_P) as computed by BurnMan. J95_RED (dashed line) and J95_OX (dotted line) compared to PREM (thick, solid line) are shown. Note the 1–1.5% difference in density between J95_RED and J95_OX.

calculated the area ratio of total alumina grains on the surface and in cross-section, and found ∼1.5% and ∼1.8%, respectively. Thus, we estimate the overall distribution of alumina grains in the whole sample is ∼1–1.2 vol%, which is ∼0.9–1.1 mol% Al_2O_3. Due to the low proportion of alumina, it would be difficult to observe its X-ray diffraction peaks. Furthermore, the overlap of Al_2O_3 XRD peaks with the abundant Bm peaks would further hide it from identification via XRD. While the proportion of exsolved alumina includes nearly all of the initial aluminium concentration (∼1.2 mol%, Supplementary Table 1), it does suggest that some Al dissolved into the Bm. Indeed, both sets of samples include Al in their Bm compositions as determined by EPMA (Supplementary Table 3). Bm has two sites for cations in the structure, that is, the 8–12 coordinated A site, and the octahedrally coordinated B site. Due to the preference of Al^{3+} to occupy the B site[17], the absorption of Al in Bm is more difficult when there is not enough Fe^{3+} available. In the J95_RED sample, the higher exsolution of stishovite causes a deficit in Si^{4+}, and Fe^{3+} will prefer to go into the B site when Mg > Si, which will cause even less Fe^{3+} to go to the A site. Similar observations were reported previously that Al_2O_3 corundum was identified by ^{27}Al NMR in more reduced samples[17]. Using the EPMA results to determine cation proportions, we roughly constrained the ferric iron abundance on the quenched samples (Methods). It shows a ferric iron to total iron ratio ($Fe^{3+}/\sum Fe$) of ∼0.36 ± 0.10, with no Fe^{3+} on the B site for the J95_OX samples, and $Fe^{3+}/\sum Fe = \sim 0.20 \pm 0.05$ for the J95_RED samples (Supplementary Table 3).

We plot the densities of Bm at ambient conditions as a function of Fe content (with three oxygen) (Fig. 3), based on previous studies on Bm with dominant ferrous or ferric iron[18–24]. It suggests that Bm with dominant Fe^{2+} exhibits a more pronounced increase in density with increasing iron content than those with mainly Fe^{3+}. Therefore, substitution of Fe^{2+} on the A site will increase the density of Bm significantly. On the other hand, although incorporation of Fe^{3+} will also increase the density, the substitution of Fe^{3+} (0.785 Å) for Si^{4+} (0.54 Å) will induce a larger increase in site radius and expand the unit cell. Besides, substitution of Fe^{3+} at the A site would be preferred at high iron content, coupled with Mg vacancies, and would lead to significant distortion of the dodecahedral site as shown by Mössbauer spectroscopy[21]. Thus, substitution of Fe^{3+} would diminish the density increase compared to the same amount of Fe^{2+} substitution.

Linking redox state to density and seismic velocities

On the basis of our XRD and EPMA results, we consider all phases present, their proportions and equations of state (Supplementary Table 4), and calculate the whole-rock densities of the two sets of samples using BurnMan[25] at lower-mantle pressures along a geotherm[26]. Due to the exsolution of stishovite and alumina, the amount of iron per formula unit of Bm in the J95_RED sample is higher than that of J95_OX sample. Given the relative low abundance of alumina and silica phases, their contributions are minimal to the bulk density of each sample. Thus, although the volume of Bm in the J95_OX samples is ∼0.4% smaller than the J95_RED samples, the overall density of the J95_RED samples is ∼1–1.5% greater than J95_OX (Fig. 4). The Preliminary Reference Earth Model (PREM)[27] is drawn for comparison, and we find that both compositions are denser than PREM (Fig. 4).

Although the densities of the J95 samples are higher than that of PREM, the P-wave speed nearly fits PREM (slower by ∼1%), while the S-wave velocity is about 1–6% slower than the PREM model within the lower-mantle pressure range (Fig. 4). Compared with seismic observations, data suggest that two broad regions with lowered shear-wave speeds and higher than average density lie beneath the Pacific and Africa[28]. Those areas have been considered to be generated by different mantle compositions (iron-rich) or chemical stratification[29]. While the enstatite chondrite lower-mantle composition[12] would not be a good estimate for bulk mantle composition, due to the intrinsic high density, it may be a candidate for the large low-shear velocity provinces (LLSVPs) along the core–mantle boundary (CMB), given its low seismic velocities.

Geodynamical numerical simulations

In spite of the relatively higher density of the J95 samples compared with the current 1-D seismically derived density of the mantle, the density difference based on the redox state is noteworthy: redox state of the mantle may affect the density of the material despite nearly identical compositions. To understand how the density difference between the reduced and oxidized material would contribute to mantle convection and evolution, we performed geodynamical numerical simulations. As a simplified case, we modelled the Earth with chondritic building blocks, composed of oxidized and reduced

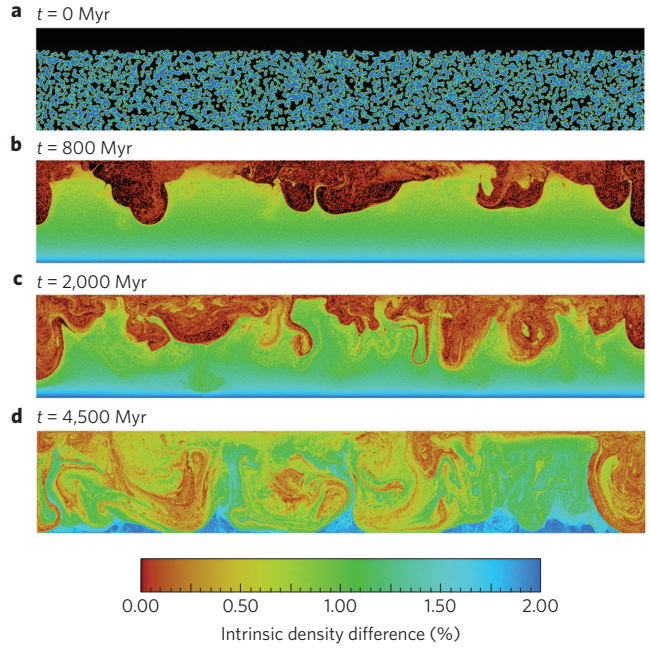

Figure 5 | Process of segregation between reduced and oxidized material caused by intrinsic density differences. a–d, Composition field in chronological order (*t*, time). Red and blue parts represent reduced and oxidized compositions with ~1.5–2% density difference, while the black part represents the upper mantle with constant density with the same value as the initial density of the more oxidized material. The colour bar represents an intrinsic density difference of 0–2%, corresponding to buoyancy number *B* between 0 and 0.8.

material with equal volumes. Random spheres of various size were introduced as the initial condition of the model, representing more reduced materials as ~2% (Fig. 5a) or ~1.5% (Fig. 6b) denser than their oxidized counterparts. To explore the effects of other factors on our geodynamic calculations, such as initial radii of reduced spheres and mantle viscosity, we also performed several different models with verified initial conditions (Methods and Fig. 6). We find consistently in our models that the redox-induced density difference can lead to rapid segregation between reduced and oxidized materials, with the oxidized and less dense material rising quickly (red to yellow regions, Fig. 5b), and the reduced and denser material sinking to the CMB (blue regions, Fig. 5b). Meanwhile, the moderately reduced material (green regions, Fig. 5c) is also continuously entrained into the upper mantle by hot upwelling mantle plumes. Furthermore, the highly reduced material (blue regions, Fig. 5d) remains stable in the lowermost mantle, and is pushed into dense thermochemical piles by cold downwellings, reminiscent of LLSVPs which have been revealed by seismic tomography[29].

Linking the deep Earth and the atmosphere

Our model shows that the oxidized (less dense) material tends to rise to the upper mantle before the slow entrainment of reduced (more dense) material (Fig. 5), which would facilitate the rise of oxygen in the atmosphere with buffer reactions that consume more reduced compositions in the early atmosphere, thereby allowing O_2 to be accumulated. It shows that the upper mantle can be oxidized in its early history (~800 Myr, Fig. 6), which is consistent with the V, Sc and Cr abundance in ancient volcanic rocks indicating that the upper mantle reached its present-day oxidation state at least ~3.6 Gyr ago[6,30,31]. The model also implies that the redox distribution in Earth's interior could be heterogeneous. While the upper part of the mantle is predominantly oxidized, the deep lower mantle, especially near the thermochemical piles (that is, LLSVPs) along the CMB, is more reduced (Fig. 5d). This is consistent with geochemical observations that the fO_2 of cratonic kimberlites is much lower than other volcanic rocks; the former is above the

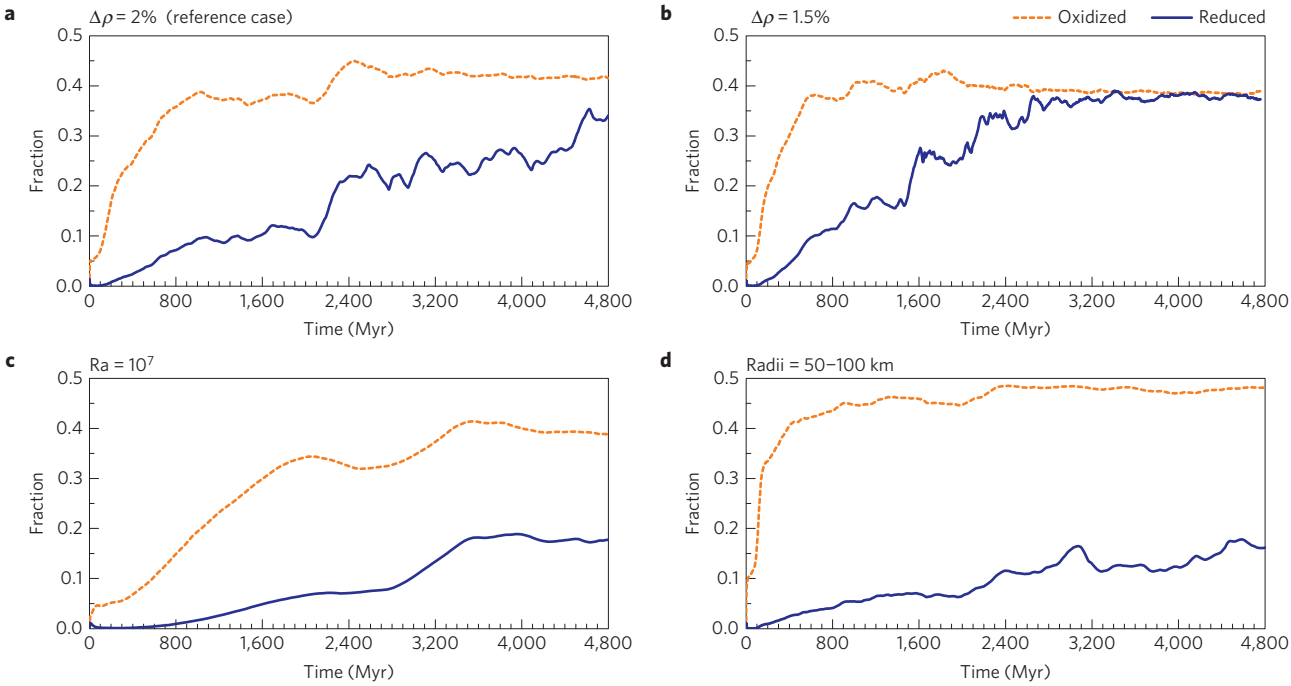

Figure 6 | Fraction of oxidized (orange, dashed) and reduced (blue, solid) material entrained into the upper mantle for four different models. **a**, Reference model with intrinsic density difference ($\Delta\rho$) up to 2% ($B = 0.8$), Rayleigh number (Ra) $= 1 \times 10^8$, and initial radii (R) of reduced spheres of 25–50 km. **b**, Same model as the reference model except with an intrinsic density difference up to 1.5% ($B = 0.6$). **c**, Same model as the reference model except Ra $= 1 \times 10^7$. **d**, Same model as the reference model except $R = 50$–100 km.

plume-generation zones at CMB, usually thought to be along the edges of LLSVPs[32]. With fO_2 below FMQ −3.5, those volcanic emissions (such as CH_4; ref. 7) have a capacity to react with O_2 and balance the oxidation state of the upper mantle to make it relatively constant[31] (Figs 5c and 6). The simulation also does not exclude the possibility that some parts of the upper mantle can be reduced, as suggested by peridotite xenoliths[7] indicating 4 ± 5 log units lower fO_2 than their source region. Besides, calculations show that the GOE requires as low as a 0.5 log unit increase in volcanic gases[4]; thus a small increase in fO_2 in the upper mantle could have a profound effect on the oxidation of the atmosphere.

Our model provides new and complementary insights into the heterogeneous oxidizing of the upper mantle and atmosphere. Although our geodynamic simulations are based on an enstatite chondrite lower-mantle composition, the crystal chemical behaviour of iron in Bm under different fO_2 should be expected in other mantle composition models. While there are several possible chemical models of the lower mantle[33], Bm is nevertheless considered the most dominant phase (above 75%) in the lower mantle; thus, its crystal chemical behaviour has a leading role in shaping the mantle's redox state. We foresee that combining our geodynamic model with information from other redox-sensitive minerals, cycles of various volatiles, and evidence from ancient mantle xenoliths will help us better understand of the fate of redox in our planet.

Methods

Methods, including statements of data availability and any associated accession codes and references, are available in the online version of this paper.

Received 20 January 2016; accepted 27 June 2016; published online 1 August 2016

References

1. Brocks, J. J., Logan, G. A., Buick, R. & Summons, R. E. Archean molecular fossils and the early rise of eukaryotes. *Science* **285,** 1033–1036 (1999).
2. Crowe, S. A. *et al*. Atmospheric oxygenation three billion years ago. *Nature* **501,** 535–538 (2013).
3. Planavsky, N. J. *et al*. Evidence for oxygenic photosynthesis half a billion years before the Great Oxidation Event. *Nature Geosci.* **7,** 283–286 (2014).
4. Holland, H. D. Volcanic gases, black smokers, and the Great Oxidation Event. *Geochim. Cosmochim. Acta* **66,** 3811–3826 (2002).
5. Kasting, J. F., Eggler, D. H. & Raeburn, S. P. Mantle redox evolution and the oxidation state of the Archean atmosphere. *J. Geol.* **101,** 245–257 (1993).
6. Li, Z.-X. A. & Lee, C.-T. A. The constancy of upper mantle fO_2 through time inferred from V/Sc ratios in basalts. *Earth Planet. Sci. Lett.* **228,** 483–493 (2004).
7. Woodland, A. B. & Koch, M. Variation in oxygen fugacity with depth in the upper mantle beneath the Kaapvaal craton, Southern Africa. *Earth Planet. Sci. Lett.* **214,** 295–310 (2003).
8. McCammon, C. & Kopylova, M. G. A redox profile of the Slave mantle and oxygen fugacity control in the cratonic mantle. *Contrib. Mineral. Petrol.* **148,** 55–68 (2004).
9. Wood, B. J., Walter, M. J. & Wade, J. Accretion of the Earth and segregation of its core. *Nature* **441,** 825–833 (2006).
10. Frost, D. J. *et al*. Experimental evidence for the existence of iron-rich metal in the Earth's lower mantle. *Nature* **428,** 409–412 (2004).
11. Mason, B. The enstatite chondrites. *Geochim. Cosmochim. Acta* **30,** 23–39 (1966).
12. Javoy, M. The integral enstatite chondrite model of the Earth. *Geophys. Res. Lett.* **22,** 2219–2222 (1995).
13. Tschauner, O., Ma, C., Beckett, J. R. & Prescher, C. Discovery of bridgmanite, the most abundant mineral in Earth, in a shocked meteorite. *Science* **346,** 1100–1102 (2014).
14. Ballaran, T. B. *et al*. Effect of chemistry on the compressibility of silicate perovskite in the lower mantle. *Earth Planet. Sci. Lett.* **333–334,** 181–190 (2012).
15. Andrault, D., Fiquet, G., Guyot, F. & Hanfland, M. Pressure-induced Landau-type transition in stishovite. *Science* **282,** 720–724 (1998).
16. Abràmoff, M. D., Magalhães, P. J. & Ram, S. J. Image processing with ImageJ. *Biophoton. Int.* **11,** 36–43 (2004).
17. Palke, A. C., Stebbins, J. F., Frost, D. J. & McCammon, C. A. Incorporation of Fe and Al in $MgSiO_3$ perovskite: an investigation by ^{27}Al and ^{29}Si NMR spectroscopy. *Am. Mineral.* **97,** 1955–1964 (2012).
18. Catalli, K. *et al*. Spin state of ferric iron in $MgSiO_3$ perovskite and its effect on elastic properties. *Earth Planet. Sci. Lett.* **289,** 68–75 (2010).
19. Dorfman, S. M., Meng, Y., Prakapenka, V. B. & Duffy, T. S. Effects of Fe-enrichment on the equation of state and stability of $(Mg,Fe)SiO_3$ perovskite. *Earth Planet. Sci. Lett.* **361,** 249–257 (2013).
20. Fei, Y., Virgo, D., Mysen, B. O., Wang, Y. & Mao, H.-K. Temperature-dependent electron delocalization in $(Mg,Fe)SiO_3$ perovskite. *Am. Mineral.* **79,** 826–837 (1994).
21. Hummer, D. R. & Fei, Y. Synthesis and crystal chemistry of Fe^{3+}-bearing $(Mg,Fe^{3+})(Si,Fe^{3+})O_3$ perovskite. *Am. Mineral.* **97,** 1915–1921 (2012).
22. Lundin, S. *et al*. Effect of Fe on the equation of state of mantle silicate perovskite over 1Mbar. *Phys. Earth Planet. Inter.* **168,** 97–102 (2008).
23. Parise, J. B., Wang, Y., Yeganeh-Haeri, A., Cox, D. E. & Fei, Y. Crystal structure and thermal expansion of $(Mg, Fe)SiO_3$ perovskite. *Geophys. Res. Lett.* **17,** 2089–2092 (1990).
24. Wang, Y., Weidner, D. J., Liebermann, R. C. & Zhao, Y. P-V-T equation of state of $(Mg, Fe)SiO_3$ perovskite: constraints on composition of the lower mantle. *Phys. Earth Planet. Inter.* **83,** 13–40 (1994).
25. Cottaar, S., Heister, T., Rose, I. & Unterborn, C. BurnMan: a lower mantle mineral physics toolkit. *Geochem. Geophys. Geosyst.* **15,** 1164–1179 (2014).
26. Brown, J. M. & Shankland, T. J. Thermodynamic parameters in the Earth as determined from seismic profiles. *Geophys. J. R. Astron. Soc.* **66,** 579–596 (1981).
27. Dziewonski, A. M. & Anderson, D. L. Preliminary reference Earth model. *Phys. Earth Planet. Inter.* **25,** 297–356 (1981).
28. Ishii, M. & Tromp, J. Constraining large-scale mantle heterogeneity using mantle and inner-core sensitive normal modes. *Phys. Earth Planet. Inter.* **146,** 113–124 (2004).
29. Garnero, E. J. & McNamara, A. K. Structure and dynamics of Earth's lower mantle. *Science* **320,** 626–628 (2008).
30. Canil, D. Vanadium partitioning and the oxidation state of Archaean komatiite magmas. *Nature* **389,** 842–845 (1997).
31. Delano, J. W. Redox history of the Earth's interior since ~3900 Ma: implications for prebiotic molecules. *Orig. Life Evolut. Biosph.* **31,** 311–341 (2001).
32. Torsvik, T. H., Burke, K., Steinberger, B., Webb, S. J. & Ashwal, L. D. Diamonds sampled by plumes from the core–mantle boundary. *Nature* **466,** 352–355 (2010).
33. Ringwood, A. E. Chemical evolution of the terrestrial planets. *Geochim. Cosmochim. Acta* **30,** 41–104 (1966).
34. Fei, Y. *et al*. Toward an internally consistent pressure scale. *Proc. Natl Acad. Sci. USA* **104,** 9182–9186 (2007).
35. Jayaraman, A. Diamond anvil cell and high-pressure physical investigations. *Rev. Mod. Phys.* **55,** 1–44 (1983).

Acknowledgements

We thank R. Weber and S. Tumber for glass synthesis; Z. Du, A. McNamara and N. J. Planavsky for discussions; G. Amulele, J. Eckert, Z. Jiang, M. Rooks, F. Camino and Y. Yang for technical support. We thank the staff and beamline scientists at GSECARS and HPCAT—in particular, V. Prakapenka, C. Prescher and S. Tkachev. We thank L. Zhang and H. K. Mao for sharing beam time. This work was funded by an NSF CAREER grant to K.K.M.L. (EAR-0955824). M.L. is supported by the NSF grant EAR-1338810. We thank CIDER 2014 for providing this opportunity for multi-disciplinary collaboration (NSF FESD grant 1135452). FIB use was supported by YINQE (NSF MRSEC DMR 1119826) and by the Center for Functional Nanomaterials, Brookhaven National Laboratory (US DOE-BES under Contract No. DE-AC02-98CH10886). EPMA was funded by the NSF (EAR-0744154) and Yale University. Portions of this work were performed at GSECARS (NSF EAR-1128799, DOE DE-FG02-94ER14466, and NSF EAR 11-57758 for gas loading system), and HPCAT (DE-NA0001974, DE-FG02-99ER45775, with partial instrumentation funding by NSF). This research used resources of the APS, a US DOE Office of Science User Facility operated for the DOE Office of Science by ANL under Contract No. DE-AC02-06CH11357.

Author contributions

T.G. and K.K.M.L. designed the experiments and conducted the analysis; T.G. performed the experiments, and designed geodynamical models with M.L., who also performed the geodynamical simulations. C.M. performed the Mössbauer analyses and interpretation. All authors contributed in the writing of the manuscript. K.K.M.L. supervised the project.

Additional information

Supplementary information is available in the online version of the paper. Reprints and permissions information is available online at www.nature.com/reprints. Correspondence and requests for materials should be addressed to T.G.

Competing financial interests

The authors declare no competing financial interests.

Methods

Samples. Each sample consists of a glass, produced by laser levitation for increased sample homogeneity, of the desired composition (Supplementary Table 1 and Supplementary Fig. 4). The glass samples are homogeneous, and are thus an excellent choice for laser-heated samples, as variation in colour, and therefore absorbance, dictate the level of laser coupling. The oxygen fugacity and amount of Fe^{3+} were controlled by the composition of the levitating gas: for the more reduced sample J95_RED, we used 95 mol% Ar, 4 mol% CO and 1 mol% CO_2 mixture; whereas for the more oxidized sample J95_OX, we used pure O_2 gas. Mössbauer spectroscopy was carried out on each starting glass sample to check the $Fe^{3+}/\Sigma Fe$ ratio (Supplementary Fig. 1 and Supplementary Table 1). Since glass is not crystalline, the oxygen content is not constrained by mineral stoichiometry, and vacancies can be developed to achieve charge balance. Therefore, although the $Fe^{3+}/\Sigma Fe$ ratio gives a fairly similar value, the oxygen content should be directly linked to the initial redox conditions.

High-pressure and high-temperature experiments. We used LHDACs equipped with 300 and 200 μm culets for intermediate (30–60 GPa) and high-pressure (50–90 GPa) experiments, respectively. Rhenium gaskets were pre-indented to 24–30 μm with a hole of 80–150 μm in diameter drilled for a sample chamber. The glass samples were powdered and loaded into the chamber. To obtain good insulation between our sample and the diamond anvils, we used stepped anvils[36] to press the powdered glass into an even foil in the centre of the chamber, while separated from the diamond anvils from both sides with a gap of 5 or 7 μm for the 200 and 300 μm culets, respectively. The sample was then loaded with Ar or Ne, which served as a pressure-transmitting medium, thermal insulation, as well as pressure calibrant[34,35].

For each synthesized J95 sample, we ran numerous sets of experiments spanning several pressure ranges of 30–60 GPa, 50–70 GPa and around 70–90 GPa. At the starting point of each target pressure range, the sample was laser heated with a defocused beam (~30 μm in diameter) on both sides and temperature was measured by two-dimensional, four-colour multi-wavelength imaging radiometry[37]. The large beam size reduces the inherent temperature gradients in the sample as well as minimizes significant iron diffusion. To verify that Soret diffusion of iron was minimal (if any), several samples were cut in cross-section by focused ion beam (FIB) (Fig. 2). The whole sample was laser heated by rastering across each sample for about 15 min to ensure full transformation of the starting glass samples to their equilibrium, crystalline assemblages, while minimizing the chance of Soret diffusion caused by prolonged heating. The sample temperature was controlled by adjusting the laser power and laser focus, keeping the peak temperatures within ~50 K on each side. After quench, the pressure was measured by Raman spectroscopy of the diamond culet[38]. The pressure, temperature and heating duration for each sample are listed in Supplementary Table 2.

Synchrotron X-ray diffraction. Room-temperature, angular-dispersive X-ray diffraction (XRD) experiments were carried out at GSECARS 13 IDD ($\lambda = 0.3344$ Å) and HPCAT 16 IDB ($\lambda = 0.3544$ Å), APS, using a highly collimated X-ray beam (3 × 4 μm) that was aligned with the centre of the sample chamber in the LHDAC. Diffraction patterns were recorded with a high-resolution MarCCD area detector and integrated with the Fit2D software[39]. The detector tilting and the distance between the sample and detector were calibrated against the known lattice parameters of LaB_6. Each synthesized sample was compressed in small pressure steps at room temperature, and XRD patterns were collected *in situ*. Each sample was decompressed to ambient conditions and further X-rayed. To better constrain the lattice parameters of each phase, we employed full-profile refinement using the Rietveld method for samples quenched from ambient conditions and the Le Bail method for data collected at high pressures with GSAS software[40,41]. Lattice parameters for stishovite at ambient conditions obtained from J95_RED (synthesized at 30 GPa) are $a = 4.188(2)$ Å, $c = 2.669(1)$ Å, $V = 46.81(4)$ Å^3 and are in good agreement with lattice parameters of pure stishovite by a single-crystal study[42], $a = 4.1801(6)$ Å, $c = 2.6678(6)$ Å, $V = 46.615(16)$ Å^3. The obtained unit-cell volume parameters of Bm under each pressure were fitted with a third-order Birch–Murnaghan equation of state (EOS) (Supplementary Table 4).

$$P = \frac{3}{2}K_0\left[\left(\frac{V_0}{V}\right)^{7/3} - \left(\frac{V_0}{V}\right)^{5/3}\right] \times \left\{1 - \frac{3}{4}(4 - K_0') \times \left[\left(\frac{V_0}{V}\right)^{2/3} - 1\right]\right\}$$

where V_0, K_0, and K_0', are the zero-pressure volume, isothermal bulk modulus, and pressure derivative of the isothermal bulk modulus, respectively.

Chemical analyses and estimating Fe^{3+} abundance in Bridgmanite. The recovered samples were analysed by scanning electron microscopy (SEM: Phillips XL-30 ESEM) or electron probe microanalysis (EPMA: JEOL JXA-8530F) in the Yale University Department of Geology and Geophysics. To investigate the homogeneity of the synthesized products, samples were investigated both in map view and in cross-section. Images were processed by NIH ImageJ[16] to calculate the area ratio of total alumina grains on the surface and in cross-section. We used the FIB to cut the samples in cross-section (for example, ref. 43) and samples were coated with carbon and analysed by energy- or wavelength-dispersive spectroscopy (EDS or WDS) to determine chemical composition. All images and elemental data were collected at an accelerating voltage of 15 kV. Quantitative microscale chemical analyses were conducted with the JEOL EPMA-system software. Counts were collected by wavelength-dispersive X-ray spectrometry (WDS) using thallium acid pthalate (TAP), pentaerythritol (PET), and lithium fluoride (LIF) diffracting crystals. Analytical conditions were 15 kV accelerating voltage, 15 nA beam current, and a focused beam, giving an approximate analytical volume of ~1.5 μm. X-ray counts were acquired for 20 or 40 s on peak and 10 or 20 s at each of the two background positions. X-ray intensities were referenced to silicate, oxide, and metallic standards, with ZAF matrix corrections applied (Z: atomic number, A: absorption, F: fluorescence). Stoichiometric oxygen was assigned to calculated elemental concentrations for matrix-correction calculations and oxide-format display. Matrix-correction calculations converged with iterations of five cycles. The precision is better than ±0.1% for the analysed elements.

We use the EPMA results on the cation proportions to roughly constrain the ferric iron abundance. We calculate the cations based on the EPMA results by apportioning the cations to the A and B sites. As previous work has established that Al prefers the B site and Fe^{3+} prefers the A site[17,44], each can occupy either site depending on the other cations. As such, for the J95_OX samples, we assign Si and Al to the B site and adjust $Fe^{3+}/\sum Fe$ appropriately to maintain charge balance. This results in a $Fe^{3+}/\sum Fe$ ratio of 0.36 ± 0.10 with no Fe^{3+} on the B site. For the J95_RED samples, the same approach does not work because the Si^{4+} and Al^{3+} content is too low to completely fill the B site. As such, this requires some Fe^{3+} on the B site, and thus the overall $Fe^{3+}/\sum Fe$ calculated for charge balance is 0.20 ± 0.05. While these calculations have a large uncertainty (small errors in the Si wt% translate to large errors in the $Fe^{3+}/\sum Fe$): the lower Si content of the J95_RED samples leads to a deficiency of cations on the B site that can only be made up by Fe^{3+} (as Fe^{2+} does not substitute on the B site).

Geodynamic model. The geodynamic numerical simulations are performed in a two-dimensional Cartesian geometry with an aspect ratio of 6:1. The equations of conservation of mass, momentum and energy are solved using the finite element code Citcom[45,46] under the Boussinesq approximation[4,47]. There are 1,536 and 256 elements in the horizontal and vertical directions, respectively, leading to a resolution of ~11 km per element. The model has a Rayleigh number of $Ra = 1 \times 10^8$. The temperature-dependent viscosity is expressed as $\eta_T = \exp[A(0.5 - T)]$, where $A = 9.21$ from 0 to 100 km depth and $A = 11.51$ from 100 to 2,890 km depth, leading to a maximum viscosity contrast of 10^4 and 10^5 due to changes of temperature in each depth range, respectively. We also employed a 50-fold viscosity increase from upper mantle to lower mantle. All boundaries are free slip. The temperature boundary conditions are isothermal on the top ($T = 0$) and bottom ($T = 1$), and insulating on the sides. The model is entirely heated from bottom. The compositional field is advected using ~7.9 million tracers with the ratio tracer method[48].

The initial temperature is $T = 0.8$ (non-dimensional) throughout the model, with some perturbations to enhance convection at the beginning of the calculation. The intrinsic density anomaly is scaled using the buoyancy number B, which is defined as the ratio between intrinsic density anomaly and dense anomaly caused by thermal expansion, or $B = \Delta\rho/(\rho\alpha\Delta T)$, where $\Delta\rho/\rho$ is the intrinsic density anomaly, α is the thermal expansivity (here $\alpha = 1 \times 10^{-5}$ K^{-1}) and ΔT is the temperature difference between surface and core–mantle boundary (here $\Delta T = 2{,}500$ K). The time is dimensionalized using $t = (h^2/\kappa)t'$, where t is the dimensional time, and t' is the non-dimensional time, h is the thickness of mantle (here, $h = 2{,}890$ km) and κ is thermal diffusivity (here, $\kappa = 1 \times 10^{-6}$ m^2 s^{-1}).

Figure 5a shows the compositional field of the initial condition, which is represented by effective intrinsic density anomaly. We initially introduced 5,900 reduced spheres (blue colour) in the lower mantle, with radii ranging from 25 to 50 km (Fig. 5a), while the background mantle (black colour) is more oxidized. The reduced material has a buoyancy number of $B = 0.8$, representing ~2% denser than the background mantle, which has a buoyancy number of $B = 0.0$. Initially, the reduced material is separated from the background oxidized material. However, in a convecting mantle, the reduced and oxidized material would mix with each other, and the effective intrinsic density anomaly is calculated using ratio tracer method[48] to give an average intrinsic density anomaly. The red to green colour in Fig. 5c,d thus represent regions where the intrinsic density anomaly and oxidation state are moderate. Initially, the proportion of the reduced material has been set as 50% in the lower mantle, based on recent studies which revealed that, with the reduced body about 45% of the Earth's mass, the mantle will yield higher ^{142}Nd, and enough uranium in the core to power the convection which creates Earth's magnetic field[49]. The upper mantle is initially fO_2 homogeneous, since the relationship between redox state and density is not constrained by our present experiments.

We also test the influences of mantle viscosity, density contrast between reduced and oxidized material and the initial size of redox heterogeneities on our results. We find that the timescale of entrainments is affected by these parameters; however, all models show a fast entrainment of oxidized and less dense material to the upper mantle, followed by a slow entrainment of more dense and reduced material to the upper mantle (Fig. 6).

Code availability. The code used to generate the geodynamical simulations, CitcomS, is readily available at Computational Infrastructure for Geodynamics at geodynamics.org. The specific modifications of the Citcom code are available on request through M.L. (limm001885@gmail.com). BurnMan is an open source mineral physics toolbox and is also freely available at geodynamics.org.

Data availability. The authors declare that all relevant data supporting the findings of this study are available within the article and its Supplementary Information files or available upon request from the corresponding author as well as K.K.M.L. (kanani.lee@yale.edu) and M.L. (limm001885@gmail.com, materials about geodynamical simulations).

References

36. Du, Z. *et al*. Using stepped anvils to make even insulation layers in laser-heated diamond-anvil cell samples. *Rev. Sci. Instrum.* **86,** 095103 (2015).
37. Du, Z., Amulele, G., Robin Benedetti, L. & Lee, K. K. M. Mapping temperatures and temperature gradients during flash heating in a diamond-anvil cell. *Rev. Sci. Instrum.* **84,** 075111 (2013).
38. Akahama, Y. & Kawamura, H. Pressure calibration of diamond anvil Raman gauge to 310 GPa. *J. Appl. Phys.* **100,** 043516 (2006).
39. Hammersley, A. P., Svensson, S. O., Hanfland, M., Fitch, A. N. & Häusermann, D. Two-dimensional detector software: from real detector to idealised image or two-theta scan. *High Press. Res.* **14,** 235–248 (1996).
40. Larson, A. C. & Dreele Von, R. B. *General Structure Analysis System* (*GSAS*) (Los Alamos National Laboratory, 2004).
41. Toby, B. H. EXPGUI, a graphical user interface for GSAS. *J. Appl. Crystallogr.* **34,** 210–213 (2001).
42. Ross, N. L., Shu, J. F., Hazen, R. M. & Gasparik, T. High-pressure crystal chemistry of stishovite. *Am. Mineral.* **75,** 739–747 (1990).
43. Du, Z. & Lee, K. K. M. High-pressure melting of MgO from (Mg,Fe)O solid solutions. *Geophys. Res. Lett.* **41,** 8061–8066 (2014).
44. Stebbins, J. F., Kojitani, H., Akaogi, M. & Navrotsky, A. Aluminum substitution in $MgSiO_3$ perovskite: investigation of multiple mechanisms by ^{27}Al NMR. *Am. Mineral.* **88,** 1161–1164 (2003).
45. McNamara, A. K., Garnero, E. J. & Rost, S. Tracking deep mantle reservoirs with ultra-low velocity zones. *Earth Planet. Sci. Lett.* **299,** 1–9 (2010).
46. Moresi, L., Zhong, S. & Gurnis, M. The accuracy of finite element solutions of Stokes' flow with strongly varying viscosity. *Phys. Earth Planet. Inter.* **97,** 83–94 (1996).
47. Li, M., McNamara, A. K. & Garnero, E. J. Chemical complexity of hotspots caused by cycling oceanic crust through mantle reservoirs. *Nature Geosci.* **7,** 366–370 (2014).
48. Tackley, P. J. & King, S. D. Testing the tracer ratio method for modeling active compositional fields in mantle convection simulations. *Geochem. Geophys. Geosyst.* **4,** 8302 (2003).
49. Wohlers, A. & Wood, B. J. A Mercury-like component of early Earth yields uranium in the core and high mantle ^{142}Nd. *Nature* **520,** 337–340 (2015).